SCIENTIFIC REPORTS

OPEN

Second-order topological insulators and loop-nodal semimetals in Transition Metal Dichalcogenides XTe_2 (X = Mo, W)

Received: 9 November 2018
Accepted: 4 March 2019
Published online: 27 March 2019

Motohiko Ezawa

Transition metal dichalcogenides XTe_2 (X = Mo, W) have been shown to be second-order topological insulators based on first-principles calculations, while topological hinge states have been shown to emerge based on the associated tight-binding model. The model is equivalent to the one constructed from a loop-nodal semimetal by adding mass terms and spin-orbit interactions. We propose to study a chiral-symmetric model obtained from the original Hamiltonian by simplifying it but keeping almost identical band structures and topological hinge states. A merit is that we are able to derive various analytic formulas because of chiral symmetry, which enables us to reveal basic topological properties of transition metal dichalcogenides. We find a linked loop structure where a higher linking number (even 8) is realized. We construct second-order topological semimetals and two-dimensional second-order topological insulators based on this model. It is interesting that topological phase transitions occur without gap closing between a topological insulator, a topological crystalline insulator and a second-order topological insulator. We propose to characterize them by symmetry detectors discriminating whether the symmetry is preserved or not. They differentiate topological phases although the symmetry indicators yield identical values to them. We also show that topological hinge states are controllable by the direction of magnetization. When the magnetization points the *z* direction, the hinges states shift, while they are gapped when it points the in-plane direction. Accordingly, the quantized conductance is switched by controlling the magnetization direction. Our results will be a basis of future topological devices based on transition metal dichalcogenides.

Higher-order topological insulators (HOTIs) are generalization of topological insulators (TIs). In the second-order topological insulators (SOTIs), for instance, topological corner states emerge though edge states do not in two dimensions, while topological hinge states emerge though surface states do not in three dimensions[1–15]. The emergence of these modes is protected by symmetries and topological invariants of the bulk. Hence, an insulator so far considered to be trivial due to the lack of the topological boundary states can actually be a HOTI. Indeed, phosphorene is theoretically shown to be a two-dimensional (2D) SOTI[16]. A three-dimensional (3D) SOTI is experimentally realized in rhombohedral bismuth[17], where topological quantum chemistry is used for the material prediction[18]. Transition metal dichalcogenides XTe_2 (X = Mo, W) are also theoretically shown to be 3D SOTIs[19,20].

The tight-binding model for transition metal dichalcogenides has already been proposed, which is closely related to a type of loop-nodal semimetals[20]. A loop-nodal semimetal is a semimetal whose Fermi surfaces form loop nodes[21–25]. Especially, the Hopf semimetal is a kind of loop-nodal semimetal whose Fermi surfaces are linked and characterized by a nontrivial Hopf number[26–30]. There is another type of loop nodal-semimetals characterized by the monopole charge[21]. An intriguing feature is that loop nodes at the zero-energy and another energy form a linked-loop structure. The proposed model[20] may be obtained by adding certain mass terms to this type of loop-nodal semimetals.

It is intriguing that topological boundary states can be controllable externally. Magnetization is an efficient way to do so. Famous examples are surface states of 3D magnetic TIs[31–34], where the gap opens for out-of-plane magnetization, while the Dirac cone shifts for in-plane magnetization. Similar phenomena also occur in 2D TIs,

Department of Applied Physics, University of Tokyo, Hongo, 7-3-1, 113-8656, Japan. Correspondence and requests for materials should be addressed to M.E. (email: ezawa@ap.t.u-tokyo.ac.jp)

which can be used as a giant magnetic resistor[35]. Recently, a topological switch between a SOTI and a topological crystalline insulator (TCI) was proposed[36], where the emergence of topological corner states is controlled by magnetization direction. We ask if a similar magnetic control works in transition metal dichalcogenides.

In this paper, we investigate a chiral-symmetric limit of the original model[20] constructed in such a way that the simplified model has almost identical band structures and topological hinge states as the original one. Alternatively, we may consider that the original model is a small perturbation of the chiral symmetric model. A great merit is that we are able to derive various analytic formulas because of chiral symmetry, which enable us to reveal basic topological properties of transition metal dichalcogenides. We find that a linking structure with a higher linking number is realized in the 3D model. We also study 2D SOTIs and 3D second-order topological semimetals (SOTSMs) based on this model. Depending on the way to introduce mass parameters there are three phases, i.e., TIs, TCIs and SOTIs in the 2D model. We find that topological phase transitions occur between these phases without band gap closing. Hence, the transition cannot be described by the change of the symmetry indicators. We propose symmetry detectors discriminating whether the symmetry is preserved or not. They can differentiate these three topological phases. Furthermore, we show that the topological hinge states in the SOTIs are controlled by magnetization. When the magnetization direction is out of plane, the topological hinge states only shift. On the other hand, when the magnetization direction is in plane, the gap opens in the topological hinge states.

Result

Hamiltonians. Motivated by the model Hamiltonian[20] which describes the topological properties of transition metal dichalcogenides β-(1T′-)$MoTe_2$ and γ-(Td-)XTe_2 (X = Mo, W), we propose to study a simplified model Hamiltonian,

$$H_{\mathrm{SOTI}} = H_0 + H_{\mathrm{SO}} + V_{\mathrm{Loop}} + V_{\mathrm{SOTSM}}, \tag{1}$$

with

$$\begin{aligned} H_0 \;=\; & \Big[m + \textstyle\sum_{i=x,y,z} t_i \cos k_i\Big]\tau_z \\ & + \lambda_x \sin k_x \tau_x + \lambda_y \sin k_y \tau_y \mu_y, \end{aligned} \tag{2}$$

$$H_{\mathrm{SO}} = \lambda_z \sin k_z \tau_y \mu_z \sigma_z, \tag{3}$$

$$V_{\mathrm{Loop}} = m_{\mathrm{Loop}} \tau_z \mu_z, \quad V_{\mathrm{SOTSM}} = m_{\mathrm{SOTSM}} \mu_x, \tag{4}$$

where σ, τ and μ are Pauli matrices representing spin and two orbital degrees of freedom. It contains three mass parameters, m, m_{Loop} and m_{SOTSM}. The role of the term m_{Loop} is to make the system a loop-nodal semimetal, and that of the term m_{SOTSM} is to make the system a SOTSM. The Brillouin zone and high symmetry points are shown in Fig. 1(a). Although the band structure of the transition metal dichalcogenides is chiral nonsymmetric, the topological nature is well described by the above simple tight-binding model.

The original Hamiltonian contains two extra mass parameters and given by

$$H'_{\mathrm{SOTI}} = H_0 + H_{\mathrm{SO}} + V'_{\mathrm{Loop}} + V'_{\mathrm{SOTSM}} \tag{5}$$

with

$$V'_{\mathrm{Loop}} = m_2 \tau_z \mu_x + m_3 \tau_z \mu_z, \tag{6}$$

$$V'_{\mathrm{SOTSM}} = m_{mv1} \mu_z + m_{mv2} \mu_x. \tag{7}$$

The simplified model H_{SOTI} captures essential band structures of the original model H'_{SOTI}. Indeed, the bulk band structures are almost identical, as seen in Fig. 1(b–d). The rod band structures are also very similar, as seen in Fig. 2(a4–d4,a5–d5), where the bulk band parts are found almost identical while the boundary states (depicted in red) are slightly different. Moreover, the both models have almost identical hinge states, demonstrating that they describe SOTIs inherent to transition metal dichalcogenides XTe_2.

A merit of the simplified model is the chiral symmetry, $\{H_{\mathrm{SOTI}}(k_x, k_y, k_z), C\} = 0$, which is absent in the original model, $\{H'_{\mathrm{SOTI}}(k_x, k_y, k_z), C\} \neq 0$. Accordingly, the band structure of H is symmetric with respect to the Fermi level. Moreover, the bulk band structure is analytically solved. Here, the chiral symmetry operator is $C = \tau_y \mu_z \sigma_x$ or $C = \tau_y \mu_z \sigma_y$. Let us call the original model a chiral-nonsymmetric model and the simplified model a chiral-symmetric model.

The common properties of the two Hamiltonians H_{SOTI} and H'_{SOTI} read as follows. First, they have inversion symmetry $P = \tau_z$ and time-reversal symmetry $T = i\tau_z \sigma_y K$ with K the complex conjugation operator. Inversion symmetry P acts on H_{SOTI} as $P^{-1} H_{\mathrm{SOTI}}(\boldsymbol{k}) P = H_{\mathrm{SOTI}}(-\boldsymbol{k})$, while time-reversal symmetry T acts as $T^{-1} H_{\mathrm{SOTI}}(\boldsymbol{k}) T = H_{\mathrm{SOTI}}(-\boldsymbol{k})$. Accordingly, the Hamiltonian has the PT symmetry $(PT)^{-1} H_{\mathrm{SOTI}}(\boldsymbol{k}) PT = H_{\mathrm{SOTI}}(\boldsymbol{k})$, which implies that $H^* = H$. Second, the z-component of the spin is a good quantum number $\sigma_z = s_z$. Since we may decompose the Hamiltonian into two sectors,

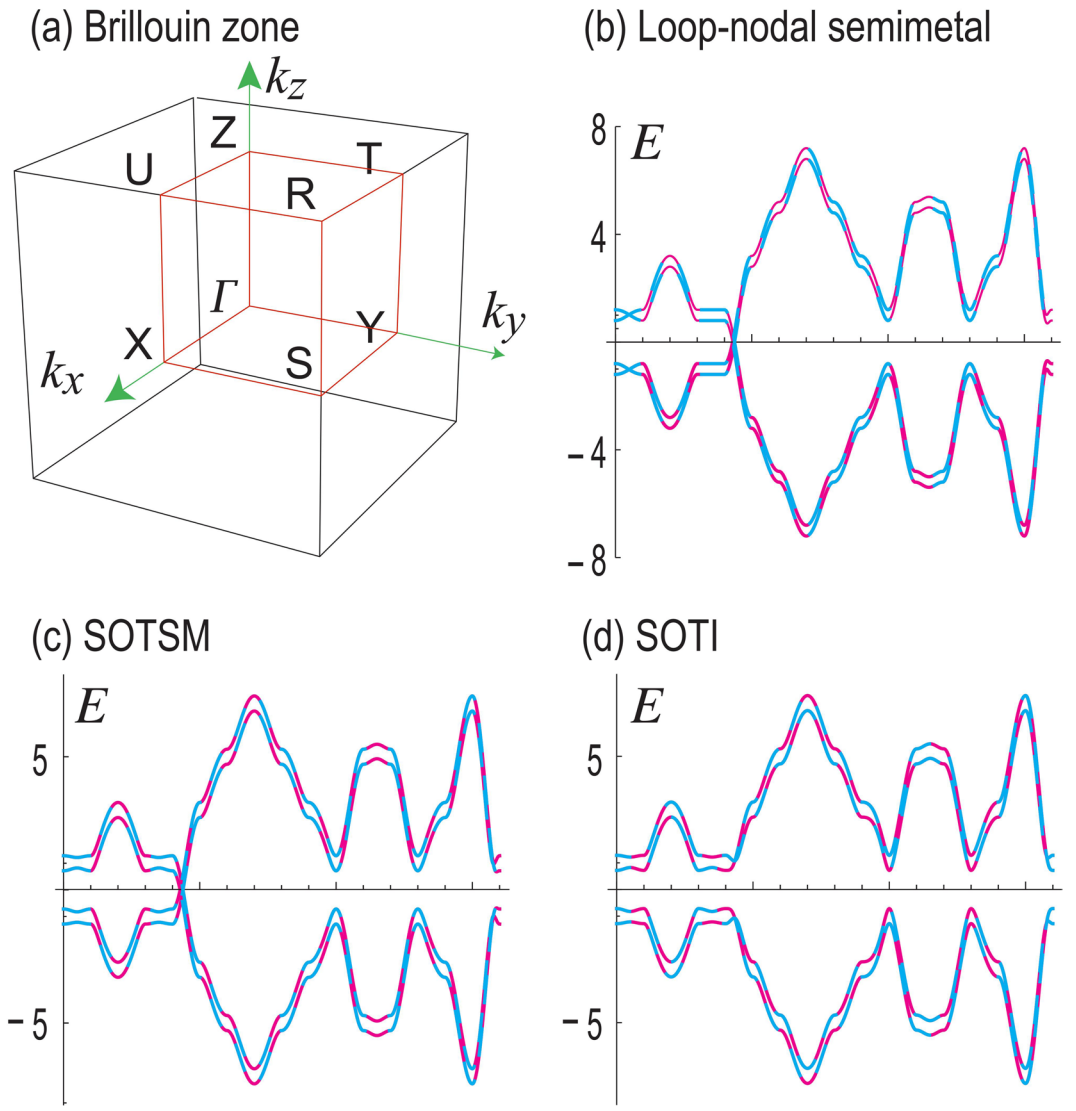

Figure 1. (**a**) Brillouin zone and high symmetry points. (**b**–**d**) Bulk band structures along the Γ-X-S-Y-Γ-Z-U-R-T-Z-Y-T-U-X-S-R-Γ line (**b**) for loop-nodal semimetal, (**c**) for SOTSM and (**d**) for SOTI. There are four bands in each phase. The dashed magenta curves represent the band structure of the chiral-symmetric model, while the dashed cyan curves represent that of the chiral-nonsymmetric model. They are indistinguishable in these figures. We have chosen $t_x = t_y = 1$, $t_z = 2$, $\lambda_x = \lambda_y = 1$, $\lambda_z = 1.2$, $m = -3$, $m_2 = 0.3$, $m_3 = 0.2$, $m_{mv1} = -0.4$, $m_{mv2} = 0.2$, $m_{\text{Loop}} = 0.3$ and $m_{\text{SOTSM}} = 0.3$.

$$H_{\text{SOTI}} = H^{\uparrow}_{\text{SOTI}} \oplus H^{\downarrow}_{\text{SOTI}}, \tag{8}$$

it is enough to diagonalize the 4×4 Hamiltonians. All these relations hold also for H'_{SOTI}. The relation (8) resembles the one that the Kane-Mele model is decomposed into the up-spin and down-spin Haldane models on the honeycomb lattice[37–39].

A convenient way to reveal topological boundary states is to plot the local density of states (LDOS) at zero energy. First, we show the LDOS for the Hamiltonian H_0 in Fig. 2(a1). It describes a Dirac semimetal, whose topological surfaces appear on the four side surfaces. Then, we show the LDOS for the Hamiltonian

$$H_{\text{Loop}} = H_0 + V_{\text{Loop}} \tag{9}$$

in Fig. 2(b1), where the topological surface states appear only on the two side surfaces parallel to the y-z plane. We will soon see that a loop-nodal semimetal is realized in H_{Loop}. Next, we show the LDOS for the Hamiltonian

$$H_{\text{SOTSM}} = H_0 + V_{\text{Loop}} + V_{\text{SOTSM}} \tag{10}$$

in Fig. 2(c1), where a SOTSM is realized with two topological hinge-arcs. Finally, by including H_{SO}, we show the LDOS for the Hamiltonian H_{SOTI} in Fig. 2(d1), where a SOTI is realized with topological two-hinge state.

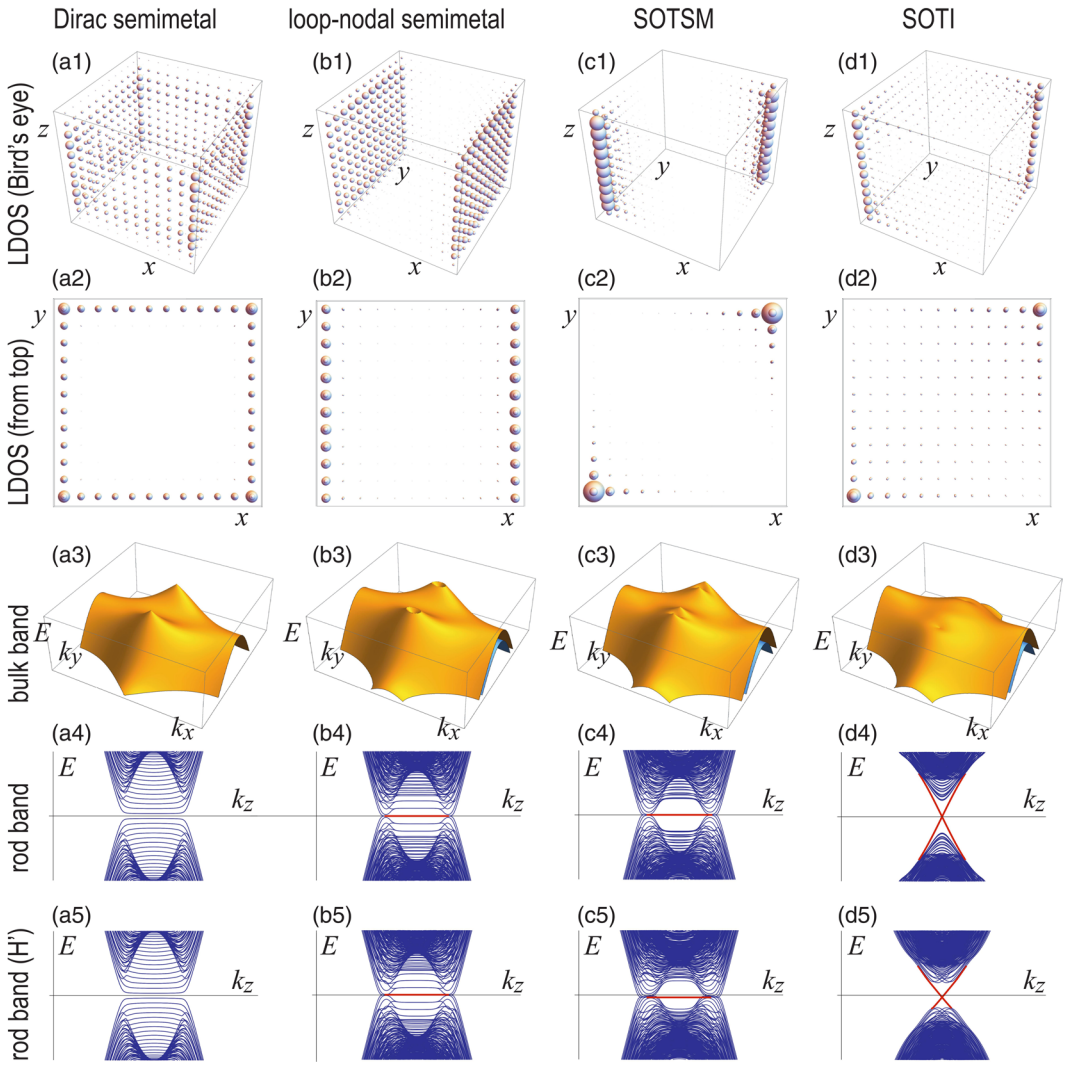

Figure 2. (**a1**–**d1**) Bird's eye's views of the LDOS of the zero-energy states: (**a1**) for H_0 with surface zero-energy states on the four side surfaces; (**b1**) for H_{Loop} with surface zero-energy states on the two side surfaces; (**c1**) H_{SOTSM} with hinge-arc states at two pillars; (**d1**) H_{SOTI} with hinge states at two pillars. (**a2**–**d2**) Top view of the LDOS corresponding to (**a1**–**d1**). (**a3**–**d3**) Bulk band structures of valence bands along $k_x = 0$ plane for these Hamiltonians. (**a4**–**d4**) Band structures of the square rod along z direction for these Hamiltonians. (**a5**–**d5**) Corresponding rod band structures for the chiral-nonsymmetric Hamiltonian H'. In these two sets of figures red curves represent topological boundary states. The Parameters are the same as in Fig. 1.

Topological phase diagram. The chiral-symmetric Hamiltonian H_{SOTI} is analytically diagonalizable. The energy dispersion is given by

$$E = \pm\sqrt{F \pm \sqrt{G}} \tag{11}$$

with

$$\begin{aligned} F &= M^2 + m_{\text{Loop}}^2 + m_{\text{SOTSM}}^2 \\ &\quad + \lambda_x^2 \sin^2 k_x + \lambda_y^2 \sin^2 k_y + \lambda_z^2 \sin^2 k_z, \end{aligned} \tag{12}$$

$$G = (m_{\text{SOTSM}} \lambda_x \sin k_x - m_{\text{Loop}} \lambda_y \sin k_y)^2 \tag{13}$$

$$+ 2M^2 (m_{\text{Loop}}^2 + m_{\text{SOTSM}}^2), \tag{14}$$

and

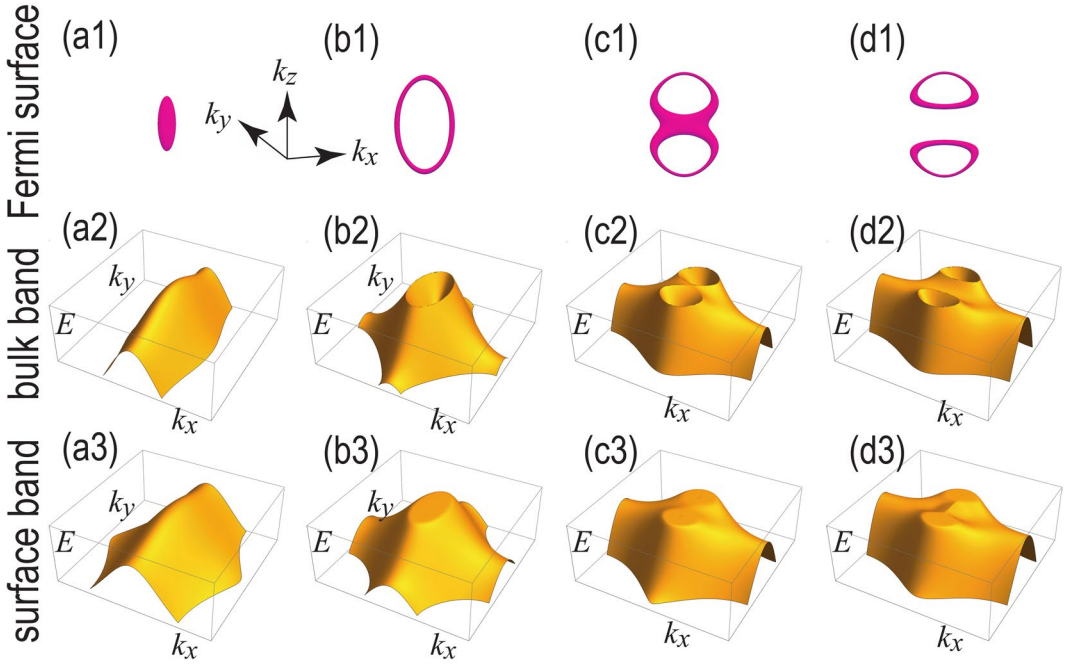

Figure 3. (**a1**–**d1**) Loop-nodal zero-energy Fermi surfaces for (**a1**) $t_z = t_1$, (**b1**) $t_1 < t_z < t_2$, (**c1**) $t_z = t_2$ and (**d1**) $t_1 < t_z < t_2$. (**a2**–**d2**) Band structures along $k_x = 0$ plane. (**a3**–**d3**) Drum-head surface states of the valence band along the y-z plane. $t_x = t_y = 1$, $\lambda_x = \lambda_y = 1$; $m = -3$, $m_{\text{Loop}} = 0.75$. In (**a2**–**d3**), only the valence bands are shown for clarity.

$$M = m + \sum_{i=x,y,z} t_i \cos k_i. \tag{15}$$

The topological phase diagram is determined by the energy spectra at the eight high-symmetry points $\Gamma = (0, 0, 0)$, $S = (\pi, \pi, 0)$, $X = (\pi, 0, 0)$, $Y = (0, \pi, 0)$, $Z = (0, 0, \pi)$, $R = (\pi, \pi, \pi)$, $U = (\pi, 0, \pi)$ and $T = (0, \pi, \pi)$ with respect to time-reversal inversion symmetry. The energies at these high-symmetry points (k_x, k_y, k_z) are analytically given by

$$E(k_i) = \eta_a M(k_i) + \eta_b \sqrt{m_{\text{Loop}}^2 + m_{\text{SOTSM}}^2}, \tag{16}$$

where $\eta_a = \pm 1$ and $\eta_b = \pm 1$. The phase boundaries are given by solving the zero-energy condition ($E = 0$),

$$(m + \eta_x t_x + \eta_y t_y + \eta_z t_z)^2 = m_{\text{Loop}}^2 + m_{\text{SOTSM}}^2, \tag{17}$$

where $\eta_x = \pm 1$, $\eta_y = \pm 1$ and $\eta_z = \pm 1$. There are 16 critical points apart from degeneracy. When $t_x = t_y$, the critical points are reduced to be 12 since $E(X) = E(Y)$ and $E(U) = E(T)$. Hence, solving $E = 0$ for t_z, there are 6 solutions for $t_z > 0$, which we set as t_n, $n = 1, 2, 3, \ldots, 6$ with $t_i < t_{i+1}$.

Loop-nodal semimetals. We first study the loop nodal phase described by the Hamiltonian H_{Loop}. The energy spectrum is simply given by

$$E = \pm \sqrt{\lambda_x^2 \sin^2 k_x + \left(\sqrt{\lambda_y^2 \sin^2 k_y + M^2} \pm \left| m_{\text{Loop}} \right| \right)^2}. \tag{18}$$

The loop-nodal Fermi surface is obtained by solving $E(\boldsymbol{k}) = 0$. It follows that $k_x = 0$ and

$$\lambda_y^2 \sin^2 k_y + M^2(0, k_y, k_z) = m_{\text{Loop}}^2. \tag{19}$$

Loop nodes at zero energy exist in the $k_x = 0$ plane. They are protected by the mirror symmetry $M_x = \tau_z \mu_z \sigma_x$ with respect to the $k_x = 0$ plane and the PT symmetry[21,40]. We show the band structure along the $k_x = 0$ plane in Fig. 3(a2–d2). We see clearly that the loop node structures are formed at the Fermi energy in Fig. 3(b2–d2). These loop nodes are also observed as the drum-head surface states, which are partial flat bands surrounded by the loop nodes as shown in Fig. 3(b3–d3). The low energy 2×2 Hamiltonian is given by

$$H = \left(\sqrt{\lambda_y^2 \sin^2 k_y + M^2} \pm \left| m_{\text{Loop}} \right| \right) \sigma_z + \lambda_x \sin k_x \sigma_x, \tag{20}$$

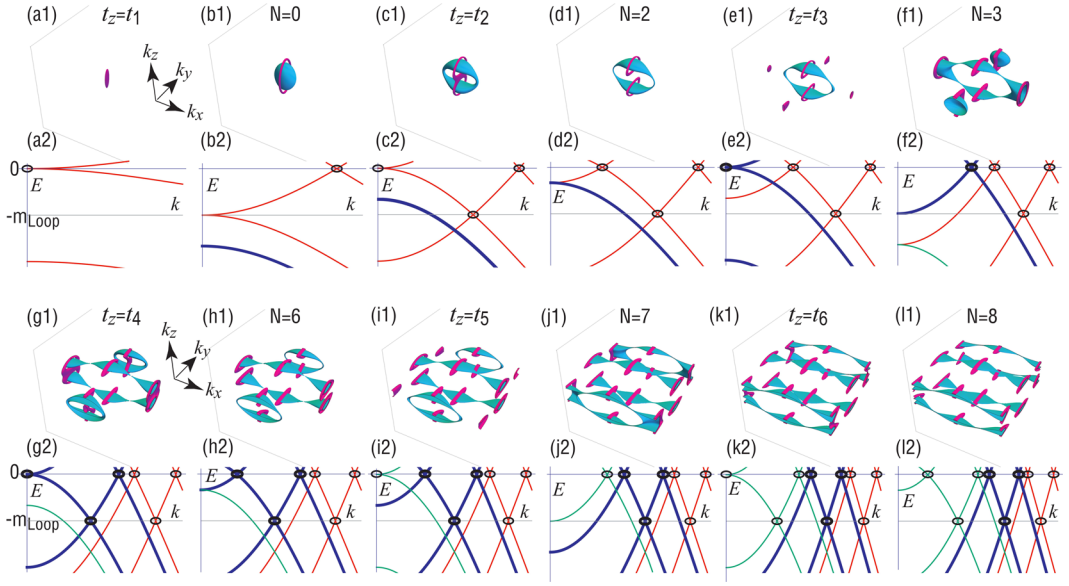

Figure 4. Evolution of linking structures for various t_z. (**a**) $t_z=t_1$, (**b**) $t_1<t_z<t_2$, (**c**) $t_z=t_2$, (**d**) $t_2<t_z<t_3$, (**e**) $t_z=t_3$, (**f**) $t_3<t_z<t_4$, (**g**) $t_z=t_4$, (**h**) $t_4<t_z<t_5$, (**i**) $t_z=t_5$, (**j**) $t_5<t_z<t_6$, (**k**) $t_z=t_6$ and (l) $t_z>t_6$. (**a1**–**l1**) Loop-nodal Fermi surfaces at the zero-energy (magenta) and at $E=-m_{\mathrm{Loop}}$ (cyan). They are linked, whose linking number N is shown in figures. (**a2**–**l2**) Band structure along the Γ-Z line (red), the X-U and Y-T lines (thick blue curves representing double degeneracy) and the S-R line (green). Only the valence bands are shown for $0\le k_z\le\pi$. Cross section of the loop nodes are marked in circles. The Parameters are the same as in Fig. 3.

where σ is the Pauli matrix for the reduced two bands.

In addition, there are loop nodes on the $k_y=0$ plane at $E=-m_{\mathrm{Loop}}$, which are determined by

$$\lambda_x^2\sin^2 k_x+(M(k_x,0,k_z)-m_{\mathrm{Loop}})^2=m_{\mathrm{Loop}}^2. \tag{21}$$

We find the two loops determined by Eqs (19) and (21) are linked, as shown in Fig. 4.

The system is a trivial insulator for $0\le t_z<t_1$. One loop emerges for $t_1<t_z<t_2$ [Fig. 3(b1)], which splits into two loops for $t_2<t_z<t_3$, as shown in Fig. 3(d1). Correspondingly, drum-head surface states, which are partial flat band within the loop nodes, appear along the [100] surface [see Fig. 3(b3,c3 and d3)].

The emergence of the loop-nodal Fermi surface is understood in terms of the band inversion[20,40], as shown in Fig. 4. The number of the loops are identical to the number of circles at the Fermi energy as in Fig. 4(a2–l2). When only one band is inverted along the Γ-Z line, a single loop node appears [Fig. 4(b1)]. When two bands are inverted along the Γ-Z line, two loop nodes appear [Fig. 4(d1)]. In the similar way, additional loops appear when additional bands are inverted along the X-U and Y-T lines [Fig. 4(f1)], and it is split into two loops [Fig. 4(h1)] as t_z increases. In the final process, a loop appears along the S-R line [Fig. 4(j1)], which splits into two loops [Fig. 4(l1)].

It has been argued[20,40] that a new topological nature of loop-nodal semimetals becomes manifest when we plot the loop-nodal Fermi surfaces at the band crossing energies, where one is at the Fermi energy and the other is at $E=-m_{\mathrm{Loop}}$ in the occupied band. We show them in Fig. 4. Along the $\Gamma-Z$ line, the other band crossing occurs at $\pm m_{\mathrm{Loop}}$ with

$$|k_z|=\arccos[(m_{\mathrm{Loop}}-m-2t)/t_z]. \tag{22}$$

Along the X-U and Y-T lines, the band crossing occurs also at $\pm m_{\mathrm{Loop}}$ with

$$|k_z|=\arccos[-m/t_z]. \tag{23}$$

Along the S-R line, the band crossing occurs also at $\pm m_{\mathrm{Loop}}$ with

$$|k_z|=\arccos[(-m+2t)/t_z]. \tag{24}$$

As a result, it is enough to plot the Fermi surfaces at $E=0$ and $E=-m_{\mathrm{Loop}}$. The linking number N increases as t_z increases, where even the linking number $N=8$ is realized as in Fig. 4(l1).

2D TI, TCI and SOTI. At this stage it is convenient to study the 2D models by setting $t_z=\lambda_z=0$. It follows from (17) that the 2D topological phase boundaries are given by

$$(m+\eta_x t_x+\eta_y t_y)^2=m_{\mathrm{Loop}}^2+m_{\mathrm{SOTSM}}^2, \tag{25}$$

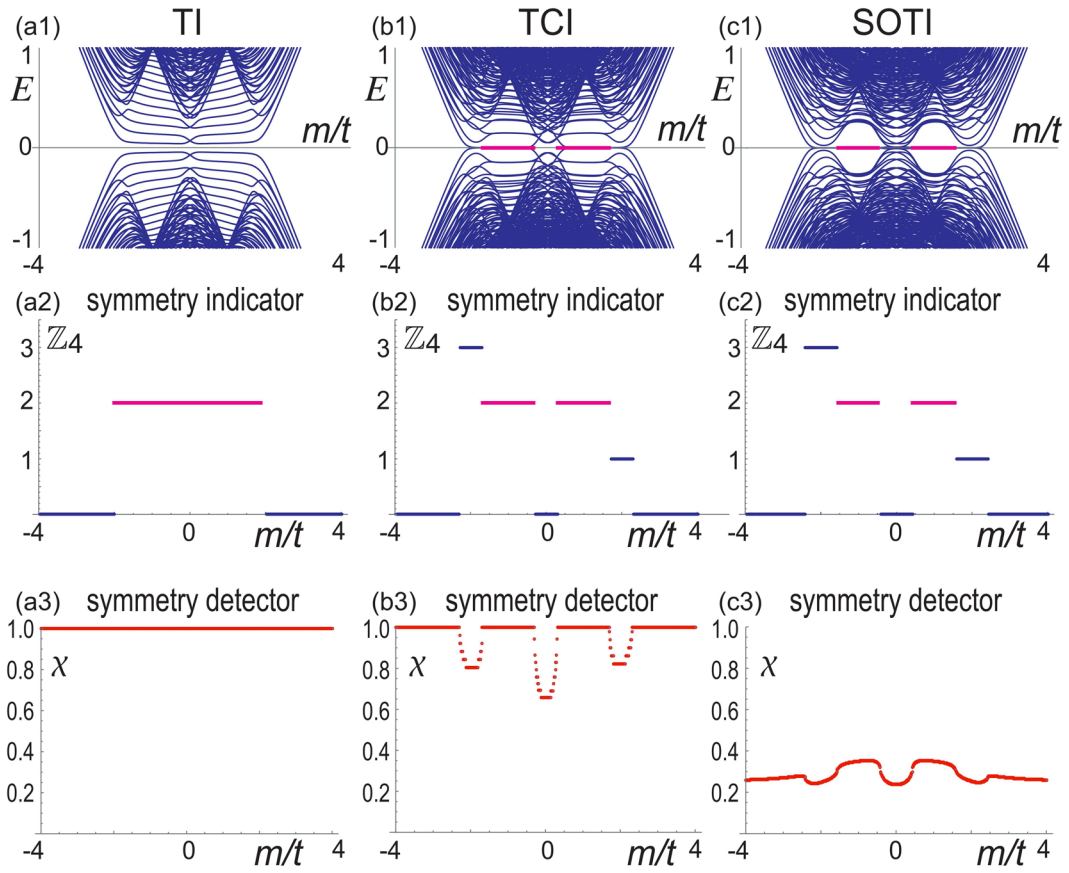

Figure 5. (**a1**–**c1**) Energy spectrum as a function of m/t for TI, TCI and SOTI phases. (**a2**–**c2**) Corresponding $\mathbb{Z}_4$ index. (**a3**–**c3**) Corresponding mirror-symmetry detector χ. It follows that $\chi = 1$ for the TI and the insulating phase of the TCI, and that $\chi \neq 1$ for the SOTI since the mirror symmetry is broken.

where $\eta_x = \pm 1$ and $\eta_y = \pm 1$. Depending on the way to introduce the mass parameters there are three phases, i.e., TIs, TCIs and SOTIs.

The topological number is known to be the $\mathbb{Z}_4$ index protected by the inversion symmetry in three dimensions[20,41–43]. This is also the case in two dimensions. It is defined by

$$\kappa_1 \equiv \frac{1}{4}\sum_{K\in \mathrm{TRIMs}}(n_K^+ - n_K^-), \tag{26}$$

where $n_K^{\pm}$ is the number of occupied band with the parity $\pm$. There is a relation[41–43]

$$\mathrm{mod}_2\kappa_1 = \nu, \tag{27}$$

where ν is the $\mathbb{Z}_2$ index characterizing the time-reversal invariant TIs. We find from Fig. 5(c1) that $\kappa_1 = 0, 2$ in the TI phase, which implies that it is trivial in the viewpoint of the time-reversal invariant topological insulators.

We show the LDOS for TI, TCI and SOTI in Fig. 6. (i) When $m_{\mathrm{Loop}} = m_{\mathrm{SOTSM}} = 0$ and $|m| < 2t$, the system is a TI with $\kappa_1 = 2$, where topological edge states appear for all edges [See Fig. 6(a)]. We show the energy spectrum and the Z_4 index in Fig. 5(a1,a2), respectively. The energy spectrum is two-fold degenerate since there is the symmetry $P\overline{T} = \mu_y$ such that $(P\overline{T})^{-1}H_0(k)P\overline{T} = H_0(k)$. Furthermore, there is the mirror symmetry $M_x = i\tau_z\mu_z$ such that $M_x^{-1}H_{\mathrm{Loop}}(k_x, k_y)M_x = H_{\mathrm{Loop}}(-k_x, k_y)$. (ii) When $m_{\mathrm{Loop}} \neq 0$ and $m_{\mathrm{SOTSM}} = 0$, the system is a TCI, where topological edge states appear only for two edges [See Fig. 6(b)]. The energy spectrum and the Z_4 index are shown in Fig. 5(b1,b2). The symmetry $P\overline{T}$ is broken for $m_{\mathrm{Loop}} \neq 0$ and the two-fold degeneracy is resolved. On the other hand, the mirror symmetry M_x remains preserved. (iii) Finally, when $m_{\mathrm{Loop}} \neq 0$ and $m_{\mathrm{SOTSM}} \neq 0$, the system is a SOTI, where two corner states emerge [See Fig. 6(c)]. The energy spectrum and the Z_4 index are shown in Fig. 5(c1,c2). The mirror symmetry is broken in the SOTI phase. In TCI and SOTI phases, there are regions where $\kappa_1 = 1, 3$. However, in this region, the system is semimetallic and the κ_1 index has no meaning.

The Z_4 index takes the same value for the TI, TCI and SOTI phases, and hence it cannot differentiate them. Indeed, because there is no band gap closing between them[44], the symmetry indicator cannot change its value[43]. A natural question is whether there is another topological index to differentiate them. We propose the symmetry detector discriminating whether the symmetry is present or not.

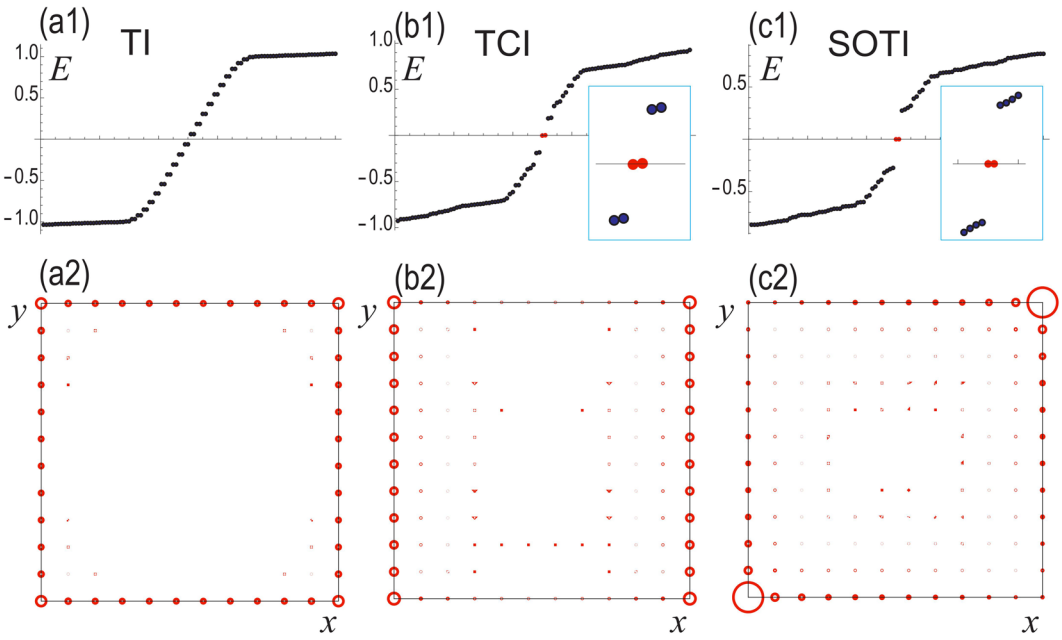

Figure 6. (**a1**–**c1**) Eigenvalues of the sample in a square geometry, where the insets show the zero-energy states in red. The vertical axis is the energy. (**a2**–**c2**) corresponding LDOS of the zero-energy states. The amplitude is represented by the radius of the circles. We have set $t_x = t_y = m = \lambda = 1$ and $m_{\text{Loop}} = m_{\text{SOTSM}} = 0.3$.

The TI and TCI are differentiated whether the symmetry $P\overline{T}$ is present or not. The band is two-fold degenerate due to the symmetry $P\overline{T}$ in the TI phase, where we can define a topological index by

$$\zeta = \text{Mod}_4 \sum_{K \in \text{TRIMs}} \frac{\text{Pf}[w]}{\sqrt{\det[w]}} \tag{28}$$

with

$$w_{ij} = \langle \psi_i(-K) | P\bar{T} | \psi_j(K) \rangle, \tag{29}$$

where i and j are the two-fold degenerated band index. It is only defined for the TI phase, where it gives the same result as κ_1. On the other hand, it is ill-defined for the TCI and SOTI phases since there is no band degeneracy.

The TCI and SOTI are differentiated by the mirror-symmetry detector defined by

$$\chi \equiv \chi_0^+ \chi_\pi^+ \chi_0^- \chi_\pi^-, \tag{30}$$

where

$$\chi_\alpha^\pm \equiv \frac{-i}{2\pi} \int_0^{2\pi} \langle \psi | M_x | \psi \rangle dk_y \Big|_{k_x = \alpha} \tag{31}$$

is the mirror symmetry indicator[36] along the axis $k_x = \alpha$ with $\alpha = 0, \pi$, and $\pm$ indicates the band index under the Fermi energy. It is $\chi = 1$ when there is the mirror symmetry. On the other hand, it is $\chi \neq 1$ when there is no mirror symmetry since $|\psi\rangle$ is not the eigenstate of the mirror operator. In addition, it is $\chi \neq 1$ when the system is metallic since $\langle \psi | M_x | \psi \rangle$ changes its value at band gap closing points. See Fig. 5(a3–c3). In Fig. 5(a3), we find always $\chi = 1$ since the mirror symmetry is preserved, where we cannot differentiate the topological and trivial phases. On the other hand, in Fig. 5(b3), there are regions with $\chi \neq 1$ where the system is metallic. Finally, we find $\chi \neq 1$ in Fig. 5(c3) since the mirror symmetry is broken.

SOTSM. A 3D SOTSM is constructed by considering k_z dependent mass term in the 2D SOTI model[10,12,13]. We set $t_z \neq 0$, while keeping $\lambda_z = 0$ in the 2D SOTI model. The properties of the SOTSM are derived by the sliced Hamiltonian $H(k_z)$ along the k_z axis, which gives a 2D SOTI model with k_z dependent mass term $M(k_z)$. The bulk band gap closes at

$$M^2(k_z) = m_{\text{Loop}}^2 + m_{\text{SOTSM}}^2. \tag{32}$$

On the other hand, there emerge hinge-arc states connecting the two gap closing points. Accordingly, the topological corner states in the 2D SOTI model evolves into hinge-states, whose dispersion forms flat bands as shown in Fig. 2(c4).

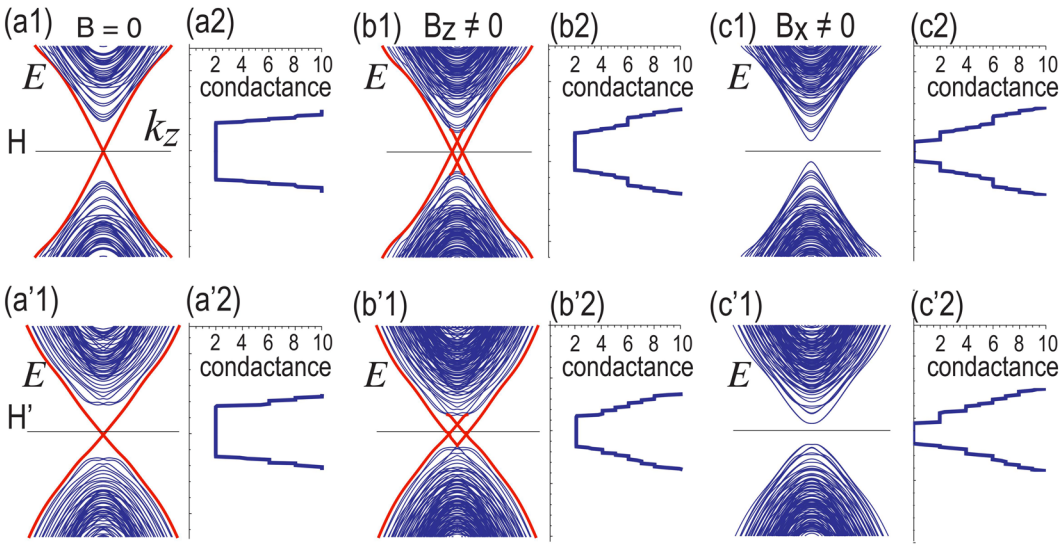

Figure 7. Band structures for hinge states (**a1**) without magnetic field, (**b1**) with magnetic field along the z direction and (**c1**) with magnetic field along the x direction for the chiral-symmetric Hamiltonian H_{SOTI}. Hinge states are depicted in red. (**a2**–**c2**) Corresponding ones for the chiral-nonsymmetric Hamiltonian H'_{SOTI}. (**a2**–**c2**) and (**a′2**–**c′2**) The conductance is quantized proportional to the number of bands in various cases.

Magnetic control of hinges in SOTI. Hinge states are analogous to edge states in two-dimensional topological insulators. Without applying external field, spin currents flow. On the other hand, once electric field is applied, charge current carrying a quantized conductance flows. We show that the current is controlled by the direction of magnetization as in the case of topological edge states.

With the inclusion of the H_{SO}, the system turns into a SOTI, which has topological hinge states. We study the effects of the Zeeman term, where the Hamiltonian is described by H_{SOTI} together with the Zeeman term

$$H_{\mathrm{Z}} = B_x\sigma_x + B_y\sigma_y + B_z\sigma_z, \tag{33}$$

which will be introduced by magnetic impurities, magnetic proximity effects or applying magnetic field.

We show the hinge states in the absence and the presence of magnetization in Fig. 7. Helical hinge states appear in its absence [see Fig. 7(a1)]. They are shifted in the presence of the B_z term [see Fig. 7(b1)]. On the other hand, they are gapped out when the B_x or B_y term exists [see Fig. 7(c1)].

For comparison, we also show the hinge states calculated from the chiral-nonsymmetric Hamiltonian H'_{SOTI} [see Fig. 7(a2–c2)]. The band structure is almost symmetric with respect to the Fermi energy.

By taking into the fact that the σ_z is a good quantum number, the low energy theory of the hinge states is well described by

$$H = \hbar v_{\mathrm{F}} k_z \sigma_z. \tag{34}$$

In the presence of the external magnetic field, it is modified as

$$H = \hbar v_{\mathrm{F}} k_z \sigma_z + B_x\sigma_x + B_y\sigma_y + B_z\sigma_z, \tag{35}$$

which is easily diagonalized to be

$$E = \pm\sqrt{(\hbar v_{\mathrm{F}} k_z + B_z)^2 + B_x^2 + B_y^2}\,. \tag{36}$$

It well reproduces the results based on the tight binding model shown in Fig. 7.

One of the intrinsic features of a topological hinge state is that it conveys a quantized conductance in the unit of e^2/h. We have calculated the conductance of the hinge states in Fig. 7 based on the Landauer formalism[45–51]. In terms of single-particle Green's functions, the conductance $\sigma(E)$ at the energy E is given by[45,51]

$$\sigma(E) = (e^2/h)\mathrm{Tr}[\Gamma_{\mathrm{L}}(E)G_{\mathrm{D}}^{\dagger}(E)\Gamma_{\mathrm{R}}(E)G_{\mathrm{D}}(E)], \tag{37}$$

where $\Gamma_{R(L)}(E) = i[\Sigma_{R(L)}(E) - \Sigma_{R(L)}^{\dagger}(E)]$ with the self-energies $\Sigma_{\mathrm{L}}(E)$ and $\Sigma_{\mathrm{R}}(E)$, and

$$G_{\mathrm{D}}(E) = [E - H_{\mathrm{D}} - \Sigma_{\mathrm{L}}(E) - \Sigma_{\mathrm{R}}(E)]^{-1}, \tag{38}$$

with the Hamiltonian H_{D} for the device region. The self energies $\Sigma_{\mathrm{L}}(E)$ and $\Sigma_{\mathrm{R}}(E)$ are numerically obtained by using the recursive method[45–51].

The conductance is quantized, which is proportional to the number of bands. When there is no magnetization or the magnetization is along the z axis, the conductance is 2 since there are two topological hinges. On the other

hand, once there is in-plane magnetization, the conductance is switched off since the hinge states are gapped. It is a giant magnetic resistor[35], where the conductance is controlled by the magnetization direction.

Conclusion

We have studied chiral-symmetric models to describe SOTIs and loop-nodal semimetals in transition metal dichalcogenides. The Hamiltonian is analytically diagonalized due to the chiral symmetry. We have obtained analytic formulas for various phases including loop-nodal semimetals, 2D SOTIs, 3D SOTSMs and 3D SOTIs. We have proposed the symmetry detector discriminating whether the symmetry is present or not. It can differentiate topological phases to which the symmetry indicator yields an identical value. Furthermore, we have proposed a topological device, where the conductance is switched by the direction of magnetization. Our results will open a way to topological devices based on transition metal dichalcogenides.

References

1. Zhang, F., Kane, C. L. & Mele, E. J. Surface State Magnetization and Chiral Edge States on Topological Insulators. *Phys. Rev. Lett.* **110**, 046404 (2013).
2. Benalcazar, W. A., Bernevig, B. A. & Hughes, T. L. Quantized electric multipole insulators. *science* **357**, 61 (2017).
3. Schindler, F., Cook, A., Vergniory, M. G. & Neupert, T. Higher-order Topological Insulators and Superconductors. *In APS March Meeting* (2017).
4. Peng, Y., Bao, Y. & von Oppen, F. Boundary Green functions of topological insulators and superconductors. *Phys. Rev. B* **95**, 235143 (2017).
5. Langbehn, J., Peng, Y., Trifunovic, L., von Oppen, F. & Brouwer, P. W. Reflection-Symmetric Second-Order Topological Insulators and Superconductors. *Phys. Rev. Lett.* **119**, 246401 (2017).
6. Song, Z., Fang, Z. & Fang, C. (d–2)-Dimensional Edge States of Rotation Symmetry Protected Topological States. *Phys. Rev. Lett.* **119**, 246402 (2017).
7. Benalcazar, W. A., Bernevig, B. A. & Hughes, T. L. Electric multipole moments, topological multipole moment pumping, and chiral hinge states in crystalline insulators. *Phys. Rev. B* **96**, 245115 (2017).
8. Schindler, F. *et al*. Higher-order topological insulators. *Science Advances* **4**, eaat0346 (2018).
9. Fang, C. & Fu, L. Rotation Anomaly and Topological Crystalline Insulators. arXiv:1709.01929 (2017).
10. Ezawa, M. Higher-Order Topological Insulators and Semimetals on the Breathing Kagome and Pyrochlore Lattices. *Phys. Rev. Lett.* **120**, 026801 (2018).
11. Geier, M., Trifunovic, L., Hoskam, M. & Brouwer, P. W. Second-order topological insulators and superconductors with an order-two crystalline symmetry. *Phys. Rev. B* **97**, 205135 (2018).
12. Lin, M. & Hughes, T. L. Topological Quadrupolar Semimetals. *Phys. Rev. B* **98**, 241103 (2018).
13. Ezawa, M. Magnetic second-order topological insulators and semimetals. *Phys. Rev. B* **97**, 155305 (2018).
14. Khalaf, E. Higher-order topological insulators and superconductors protected by inversion symmetry. *Phys. Rev. B* **97**, 205136 (2018).
15. Ezawa, M. Strong and weak second-order topological insulators with hexagonal symmetry and Z_3 index. *Phys. Rev. B* **97**, 241402(R) (2018).
16. Ezawa, M. Minimal models for Wannier-type higher-order topological insulators and phosphorene. *Phys. Rev. B* **98**, 045125 (2018).
17. Schindler, F. *et al*. Higher-order topology in bismuth. *Nature Physics* **14**, 918 (2018).
18. Bradlyn, B. *et al*. Topological quantum chemistry. *Nature* **547**, 298 (2017).
19. Tang, F., Po, H. C., Vishwanath, A. & Wan, X. Efficient Topological Materials Discovery Using Symmetry Indicators. arXiv:1805.07314 (2018).
20. Wang, Z., Wieder, B. J., Li, J., Yan, B. & Bernevig, B. A. Higher-Order Topology, Monopole Nodal Lines, and the Origin of Large Fermi Arcs in Transition Metal Dichalcogenides XTe2 (X = Mo, W). arXiv:1806.11116 (2018).
21. Fang, C., Chen, Y., Kee, H.-Y. & Fu, L. Topological nodal line semimetals with and without spin-orbital coupling. *Phys. Rev. B* **92**, 081201(R) (2015).
22. Kim, Y., Wieder, B. J., Kane, C. L. & Rappe, A. M. Dirac Line Nodes in Inversion-Symmetric Crystals. *Phys. Rev. Lett.* **115**, 036806 (2015).
23. Yu, R., Weng, H., Fang, Z., Dai, X. & Hu, X. Topological Node-Line Semimetal and Dirac Semimetal State in Antiperovskite Cu3PdN. *Phys. Rev. Lett.* **115**, 036807 (2015).
24. Chan, Y.-H., Chiu, C.-K., Chou, Y. & Schnyder, A. P. Ca3P2 and other topological semimetals with line nodes and drumhead surface states. *Phys. Rev. B* **93**, 205132 (2016).
25. Song, Z., Zhang, T. & Fang, C. Diagnosis for Nonmagnetic Topological Semimetals in the Absence of Spin-Orbital Coupling. *Phys. Rev. X* **8**, 031069 (2018).
26. Chen, W., Lu, H.-Z. & Hou, J.-M. Topological semimetals with a double-helix nodal link. *Phys. Rev. B* **96**, 041102 (2017).
27. Yan, Z. *et al*. Nodal-link semimetals. *Phys. Rev. B* **96**, 041103(R) (2017).
28. Chang, P.-Y. & Yee, C.-H. Weyl-link semimetals. *Phys. Rev. B* **96**, 081114 (2017).
29. Ezawa, M. Topological semimetals carrying arbitrary Hopf numbers: Fermi surface topologies of a Hopf link, Solomon's knot, trefoil knot, and other linked nodal varieties. *Phys. Rev. B* **96**, 041202(R) (2017).
30. Chang, G. *et al*. Topological Hopf and Chain Link Semimetal States and Their Application to Co_2MnGa. *Phys. Rev. Lett.* **119**, 156401 (2017).
31. Chen, Y. L. *et al*. Massive Dirac Fermion on the Surface of a Magnetically Doped Topological Insulator. *Science* **329**, 659 (2010).
32. Zhang, J. *et al*. Topology-Driven Magnetic Quantum Phase Transition in Topological Insulators. *Science* **339**, 1582 (2013).
33. Chang, C.-Z. *et al*. Experimental Observation of the Quantum Anomalous Hall Effect in a Magnetic Topological Insulator. *Science* **340**, 167 (2013).
34. Checkelsky, J. G. *et al*. Trajectory of the anomalous Hall effect towards the quantized state in a ferromagnetic topological insulator. *Nat. Phys.* **10**, 731 (2014).
35. Rachel, S. & Ezawa, M. Giant magnetoresistance and perfect spin filter in silicene, germanene, and stanene. *Phys. Rev. Bbf* **89**, 195303 (2014).
36. Ezawa, M. Topological Switch between Second-Order Topological Insulators and Topological Crystalline Insulators. *Phys. Rev. Lett.* **121**, 116801 (2018).
37. Kane, C. L. & Mele, E. J. Z_2 Topological Order and the Quantum Spin Hall Effect. *Phys. Rev. Lett.* **95**, 146802 (2005).
38. Ezawa, M. Monolayer Topological Insulators: Silicene, Germanene, and Stanene. *J. Phys. Soc. Jpn.* **84**, 121003 (2015).
39. Kane, C. L. & Mele, E. J. Quantum Spin Hall Effect in Graphene. *Phys. Rev. Lett.* **95**, 226801 (2005).
40. Ahn, J., Kim, Y. & Yang, B.-J. Band Topology and Linking Structure of Nodal Line Semimetals with Z_2 Monopole Charges. *Phys. Rev. Lett.* **121**, 106403 (2018).
41. Po, H. C., Vishwanath, A. & Watanabe, H. Symmetry-based indicators of band topology in the 230 space groups. *Nat. Comm.* **8**, 50 (2017).

42. Song, Z., Zhang, T., Fang, Z. & Fang, C. Quantitative mappings between symmetry and topology in solids. *Nat. Com.* **9**, 3530 (2018).
43. Khalaf, E., Po, H. C., Vishwanath, A. & Watanabe, H. Symmetry Indicators and Anomalous Surface States of Topological Crystalline Insulators. *Phys. Rev. X* **8**, 031070 (2018).
44. Ezawa, M., Tanaka, Y. & Nagaosa, N. Topological Phase Transition without Gap Closing. *Scientific Reports* **3**, 2790 (2013).
45. Datta, S. *Electronic Transport in Mesoscopic Systems* (Cambridge University Press, Cambridge, England, 1995).
46. Muñoz-Rojas, F., Jacob, D., Fernández-Rossier, J. & Palacios, J. J. Coherent transport in graphene nanoconstrictions. *Phys. Rev. B* **74**, 195417 (2006).
47. Zârbo, L. P. & Nikolić, B. K. Condensed Matter: Electronic Structure, Electrical, Magnetic and Optical Properties. *EPL* **80**, 47001 (2007).
48. Li, T. C. & Lu, S.-P. Quantum conductance of graphene nanoribbons with edge defects. *Phys. Rev. B* **77**, 085408 (2008).
49. Ezawa, M. Quantized conductance and field-effect topological quantum transistor in silicene nanoribbons. *Appl. Phys. Lett.* **102**, 172103 (2013).
50. Areshkin, D. A. & Nikolić, B. K. I-V curve signatures of nonequilibrium-driven band gap collapse in magnetically ordered zigzag grapheme nanoribbon two-terminal devices. *Phys. Rev. B* **79**, 205430 (2009).
51. Datta, S. *Quantum transport: atom to transistor* (Cambridge University Press, England, 2005).

Acknowledgements

The author is very much grateful to N. Nagaosa for helpful discussions on the subject. This work is supported by the Grants-in-Aid for Scientific Research from MEXT KAKENHI (Grant Nos JP17K05490, JP15H05854 and No. JP18H03676). This work is also supported by CREST, JST (JPMJCR16F1).

Author Contributions

M.E. conceived the idea, performed the analysis, and wrote the manuscript.

Additional Information

Competing Interests: The author declares no competing interests.

Publisher's note: Springer Nature remains neutral with regard to jurisdictional claims in published maps and institutional affiliations.